J. Fluid Mech. (2013), *vol.* 730, *pp.* 328–342.
doi:10.1017/jfm.2013.358

Drop impact on super-wettability-contrast annular patterns

Seungho Kim[1], Myoung-Woon Moon[2] and Ho-Young Kim[1,†]

[1]School of Mechanical and Aerospace Engineering, Seoul National University, Seoul 151-744, Korea

[2]Institute of Multidisciplinary Convergence of Materials, Korea Institute of Science and Technology, Seoul 136-791, Korea

(Received 11 January 2013; revised 1 July 2013; accepted 8 July 2013)

Extreme wetting properties of solids, either superhydrophobic or superhydrophilic, provide versatile methods to achieve unusual liquid deposit morphologies, such as liquid pearls or polygonal films. Here we report the dynamics of liquid drops that impact on solid surfaces where the extreme wetting properties are coupled in such a way that a superhydrophilic annulus is patterned on a superhydrophobic background. The drop that initially spreads on the inner superhydrophobic region is arrested by the hydrophilic annulus. The liquid deposit gets destabilized because of the strong water repellence of the inner region, exhibiting the burst and disengagement of the liquid film. This process leads to the formation of a liquid ring defined by the annulus pattern, which has practical implications in rapid printing of functional liquids. We visualize such drop dynamics with a high-speed camera and characterize their salient features by combining experimental measurements and theoretical considerations.

Key words: capillary flows, drops and bubbles, interfacial flows (free surface)

1. Introduction

Although the drop impact on solid surfaces has been the subject of intense study for more than a century (Worthington 1877; Rein 1993; Yarin 2006), the hydrodynamic analysis of liquid drop behaviour on surfaces with extreme wettability conditions, whether superhydrophobic or superhydrophilic, began only recently (Clanet *et al.* 2004; Ishino *et al.* 2007; Tsai *et al.* 2009; Kim *et al.* 2011*a*). In general, the wettability of microscopically rough surfaces is magnified compared to that of smooth surfaces, thus rough hydrophobic (hydrophilic) surfaces become superhydrophobic (superhydrophilic). The tailored topography of solid surfaces as well as wide range of wettability, made possible thanks to recent developments of micro- and nanofabrication technology, has enabled the formation of some novel liquid deposit shapes. On superhydrophobic surfaces, a water drop retains an almost spherical shape (Onda *et al.* 1996), whereas superhydrophilic surfaces cause drops to wick through the surface protrusions, resulting in an extremely thin film (Quéré 2008). In addition to axisymmetric deposits, polygonal spreading was observed on micropillar arrays with the detailed shape depending on the pillar wettability, distribution and dimensions

† Email address for correspondence: hyk@snu.ac.kr

(Bico, Tordeux & Quéré 2001; Cubaud & Fermigier 2001; Courbin *et al.* 2007; Sbragaglia *et al.* 2007). Still, limitations exist in achieving complicated morphologies of liquid deposit, which play important roles in the lab-on-a-chip technology (Zhang *et al.* 2011) and printable electronics (Russo *et al.* 2011).

Besides the surface topography, patterns of wettability can control the shape of a liquid deposit. Kataoka & Troian (1999) demonstrated a thermocapillary flow guided along a hydrophilic lane while the neighbouring hydrophobic region remained dry. Zhao, Moore & Beebe (2001) realized liquid streams following virtual conduits of hydrophilic lines inside microchannels. Jokinen, Sainiemi & Franssila (2008) showed that a sessile drop containing an air bubble in its interior can be generated on a superhydrophobic surface with a wettable annular pattern by slowly increasing the deposit volume. Thin spokes or narrow fans of liquids radiating from a centre were generated by drop impact on the surface with microscale wettability patterns (Lee, Chang & Kim 2010). These previous studies show that patterning the wettability of solid surfaces can provide a fairly sophisticated way to control the drop morphology.

Here we investigate the dynamic behaviour of a drop impacting on super-wettability-contrast patterns where a wettable annulus is surrounded by superhydrophobic background to effectively combine the aforementioned capabilities of extreme wettability conditions and of microwetting patterns in deposit shape control. We find hitherto unreported drop dynamics, such as spontaneous film rupture followed by liquid ejection and water annulus formation, which may lead to novel microfluidic applications. In the following, we start with a description of experimental procedures and then report the observation of different behaviours of liquid drops on the annular wettability patterns depending on the impact conditions and the annulus dimensions. We then provide hydrodynamic analyses for several salient features in the process. Finally we demonstrate the practical implications of the phenomena investigated here.

2. Experiments

We use PET (polyethylene terephthalate) substrates to fabricate super-water-repellent surfaces with wettable annular patterns. We first clean the substrate with Ar gas and then follow the steps illustrated in figure 1. We create nanoscale roughness on the surface by means of O_2 etching in a plasma-assisted chemical vapour deposition (PACVD) chamber for 30 min. Then it is coated with an amorphous $C_6H_{18}Si_2O$ film using hexamethyldisiloxane (HMDSO) gas via the PACVD process. For detailed conditions of the plasma process, see Shin *et al.* (2012). The resulting surface is covered with nanograsses as shown in figure 2, and the root-mean-square (r.m.s.) surface roughness is measured to be 150 nm with 5.3 % of standard deviation by scanning area of 25 μm^2 using an atomic force microscope (Park Systems XE-70). The surface roughness, defined as the ratio of the actual surface area to the projected area, is 1.8. To selectively hydrophilicize an annular area, the surface is spin-coated with a photoresist (AZ 1512) and exposed to ultraviolet radiation with a photomask on it. After removing the irradiated photoresist region with a developer, the photoresist-patterned substrate is treated with air plasma, which makes the exposed area superhydrophilic (Kim *et al.* 2011*b*). Finally, removing the residual photoresist with acetone, we are left with a surface with extreme wettability contrast: superhydrophilic in the air-plasma-treated annulus and superhydrophobic elsewhere. We vary the size of the annulus so that the inner radius R_i ranges between 1.5 and 5.0 mm and the outer radius R_o between 2.0 and 7.5 mm. By imaging water drops of 2 µl volume, the static contact angle θ_s of the superhydrophilic and the superhydrophobic surface is

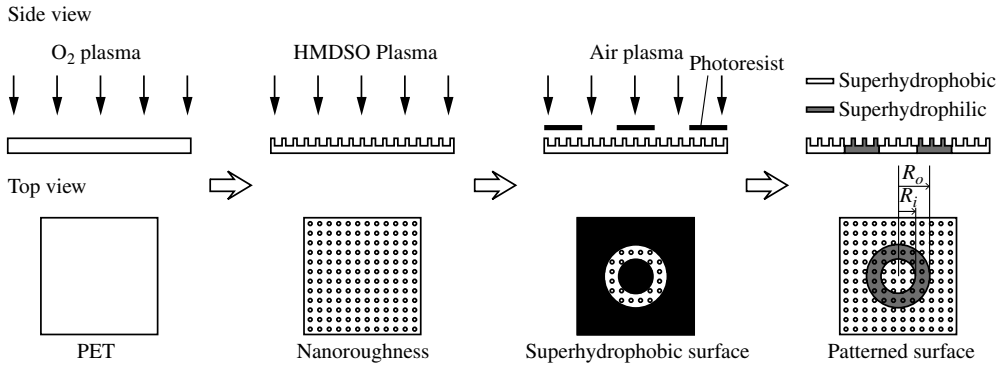

FIGURE 1. Fabrication process of the surface with extreme wettability contrast.

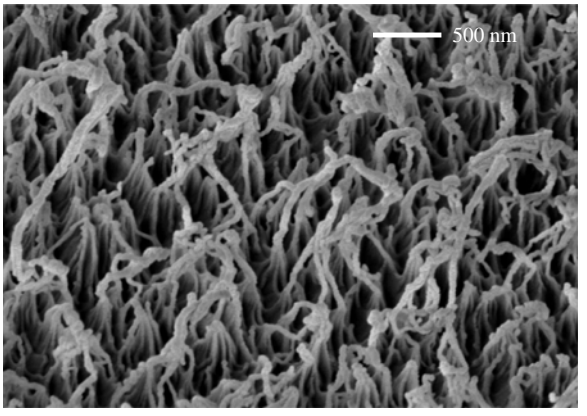

FIGURE 2. Scanning electron microscopy (SEM) image of nanograsses formed on a PET substrate.

measured to be nearly zero and $160 \pm 2°$, respectively. The critical advancing contact angle, θ_a, and the critical receding contact angle, θ_r, of the superhydrophobic surface are measured by increasing (θ_a) or decreasing (θ_r) the drop volume until the contact line starts to move with an aid of a syringe needle immersed in the drop (de Gennes, Brochard-Wyart & Quéré 2004). Then we find the contact angle hysteresis, $\theta_a - \theta_r$, to be $5° \pm 2°$.

We use deionized water emitting from a micropipette to create liquid drops of radius a ranging between 1.2 and 1.9 mm. They fall under gravity to impact on the horizontal surface. They hit the centre of superhydrophobic region surrounded by the annulus. The impact velocity of a drop, U, is varied by changing the distance it travels: U ranges between 0.44 and 2.65 m s^{-1}. The shape evolution of the drop is recorded by a high-speed camera (Photron Fastcam SA1.1) at a rate ranging between 3000 and 20 000 frames per second with a pixel resolution of 512×512. In the experiments, the substrate is located on the precision balance (Mettler Toledo XS205) to measure the temporal change of drop mass. We deduce the thickness of a thin liquid lens from its mass assuming that the lens is a part of a sphere due to negligible gravitational effects.

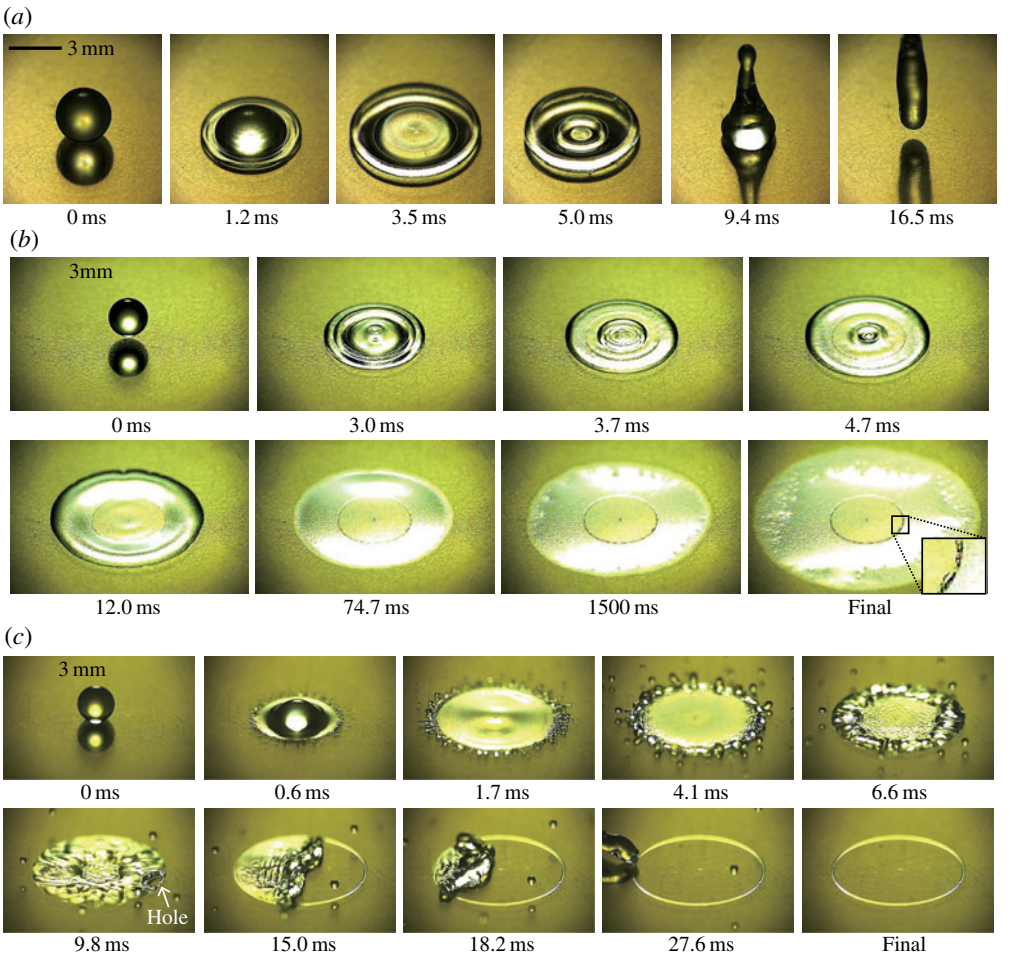

FIGURE 3. (Colour online) Different types of drop impact behaviour. (*a*) Rebound for $R_m < R_i$. (*b*) Lens formation for $R_i < R_m < R_o$. (*c*) Lens rupture, droplet ejection, and generation of a ring for $R_m > R_o$. $[R_i, R_o] = [4.0, 4.2]$ (*a*), [2.5, 7.5] (*b*) and [5.0, 5.2] mm (*c*). The impact Weber number $We = 25$ (*a*,*b*) and 106 (*c*).

3. Types of drop impact behaviour

Figure 3(*a–c*) shows different types of drop impact behaviour depending on how a liquid drop interacts with the hydrophilic annulus surrounded by the super-water-repellent background. The effects of the hydrophilic region manifest themselves only when the maximum spread radius of the drop, R_m, is greater than R_i. We first varied R_i and R_o, while the drops of $a = 1.3$ mm have impact velocity $U = 1.2$ and 2.5 m s^{-1} for (*a*,*b*) and (*c*), respectively. Thus, the Weber number $We = \rho U^2 a/\gamma = 25$ and 106 for (*a*,*b*) and (*c*), respectively. Here ρ is the liquid density and γ the surface tension. The corresponding Reynolds numbers $Re_a = \rho U a/\mu$, with μ being the viscosity, are 1560 and 3250 for (*a*,*b*) and (*c*), respectively. Clanet *et al.* (2004) showed that it is the parameter $P = 1.15We/Re_a^{4/5}$ that determines whether the impact inertia is balanced by the interfacial tension or the viscosity. In our cases with P being much smaller than

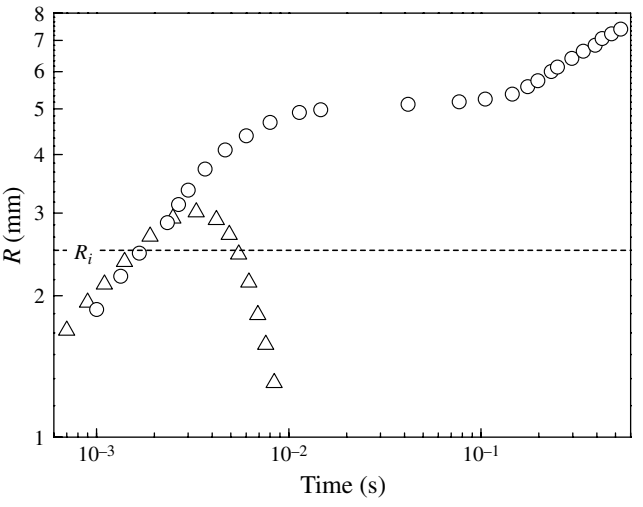

FIGURE 4. Temporal evolution of the base radius of a water drop with the initial radius $a = 1.3$ mm impacting with the speed of $U = 1.2$ m s^{-1} on a uniformly superhydrophobic surface (triangles) and a wettability-patterned surface with $R_i = 2.5$ mm (circles).

unity, the drop impact is in the capillary regime where the drop inertia is balanced with the interfacial tension.

For $R_m < R_i$, in figure 3(*a*), the water drop recoils and eventually disengages from the super-water-repellent area upon reaching the maximum radius $R_m = 3.1$ mm, which is typical of drops with $We \in [0.1\text{–}30]$ (Rioboo *et al.* 2008). In this We range, R_m is determined by the balance of inertia of the decelerated drop with the interfacial tension as $R_m/a \sim We^{1/4}$ (Clanet *et al.* 2004).

For $R_i < R_m < R_o$, the spreading front is arrested in the hydrophilic annulus, thereby allowing the drop to rest on the water-repellent surface in a thin lens shape as shown in figure 3(*b*). Although the contact line does not retract, a ridge formed around the rim returns to the centre, much like a drop impinging on a uniformly hydrophilic surface (Mao, Kuhn & Tran 1997). However, two salient flow characteristics are observed, as delineated in the following.

First, the spreading front continues to advance even as the ridge retracts (3.0–4.7 ms in figure 3*b*), unless the contact line has reached the outer edge of the hydrophilic annulus corresponding to $R_m = R_o$. Figure 4 compares the temporal evolution of the drop base radius on a uniformly superhydrophobic surface and a superhydrophobic surface with a wettable annular pattern. On the uniformly hydrophobic surface, the drop rapidly recoils upon reaching the maximum spread radius at around 3.5 ms. On the wettability-patterned surface, however, the base radius, R, plateaus after the first spreading phase that lasts till 0.01 s. In this constant-spread-radius stage, the flow induced by the inward propagation of the capillary wave of the top surface appears to balance the outward spreading driven by the high wettability of the substrate. While the contact line remains immobile, the capillary wave subsides and the drop smooths its shape into a lens. Then, the second-phase spreading (after 0.15 s) within the wettable annulus is driven by wicking of a liquid film over rough superhydrophilic surface rather than by the impact inertia.

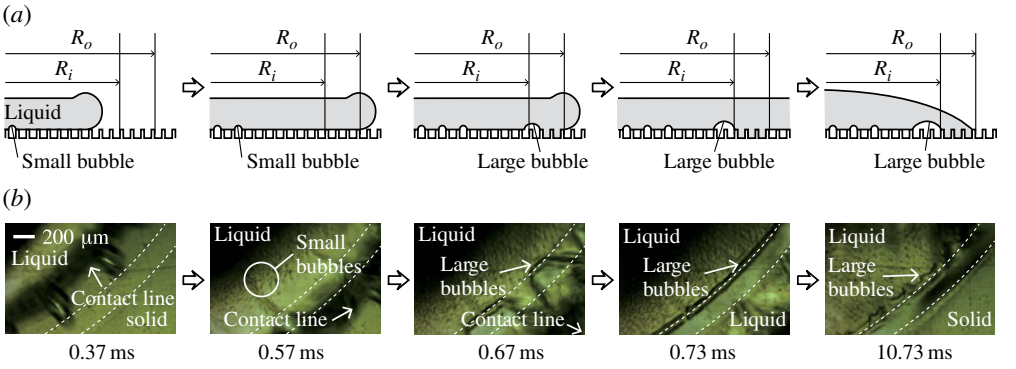

FIGURE 5. (Colour online) Air bubble entrainment during spreading. (*a*) Schematic process of entrainment of air due to instability of the contact line advancing on the hydrophobic surface and abrupt encounter of the hydrophilic region. The abrupt switch of the contact mode at the annular region from that of Cassie–Baxter to Wenzel occurs between the second and third panels, by which a large bubble is trapped. The large bubble formed at the wettability boundary (the third panel) moves into the superhydrophobic region because of a strong affinity for gas and liquid of the superhydrophobic and superhydrophilic region, respectively. In the last panel, the contact line has receded back to $R = R_o$. (*b*) Magnified images near the wettability boundary visualizing the formation process of air bubbles illustrated in (*a*). The times are measured from the moment that the drop hits the substrate. The dashed lines correspond to the inner and outer edges of the wettable annulus. The liquid front advances from the upper left to the lower right. In the last panel (10.73 ms), the small bubbles inside the inner wettability boundary are distinguished from the irregularly shaped large bubbles at the wettability boundary.

Second, microscopic air bubbles are trapped between the liquid and the superhydrophobic surface, as clearly seen in the last panel of figure 3(*b*). These tiny bubbles are formed by entrainment of air as the contact line rapidly advances. Scrutinizing the microscopic bubbles generated in this work, we find that two distinct sizes of bubbles exist: relatively small ones with radius (viewed from the top) ranging between approximately 5 and 15 μm are distributed inside the hydrophobic area, whereas larger ones are located close to the inner edge of the annulus.

The small bubbles are generated because the contact line advancing on a hydrophobic surface becomes unstable and roughened (Blake & Ruschak 1979; Eggers 2004) when its speed exceeds a critical value, U_c, which is predicted to be $U_c = c\gamma(\pi - \theta_A)^3/\mu$ (Duez *et al.* 2007), where c is a constant of the order of 10^{-2}. Substituting the properties of water and $\theta_A \approx 160°$, we find that U_c ranges between 10^{-2} and 10^{-1} m s^{-1}, which is significantly lower than the typical spreading speed of the contact line in this work, $\sim$1 m s^{-1}. Therefore, the unstable contact line roughens to entrain small air bubbles until it meets the hydrophilic annulus. The process is schematically illustrated in the first two panels of figure 5(*a*) with the corresponding images shown in (*b*). The small bubbles with a circular top view hardly change their shapes with time. On the other hand, the formation of relatively large bubbles begins when the contact line encounters the boundary of the hydrophobic–hydrophilic regions (R_i), the second and third panels of figure 5(*a*,*b*). A strip of bubbles is trapped at the boundary while the abrupt change of the liquid–solid contact mode from that of Cassie & Baxter (1944) to Wenzel (1936) occurs. We suppose that the air flow through the forest of nanopillars following the liquid flow (Cassie–Baxter state) is trapped at

the wettability boundary as the liquid suddenly starts to intimately contact the rough hydrophilic area (Wenzel state). The detailed dynamics of this air trapping process leading to formation of large bubbles is worth further study, but is not pursued further here. The annular air strip in 0.73 ms of figure 5(*b*) evolves into a series of relatively large bubbles by capillary action, as shown in the fourth to fifth panels in figure 5(*b*). The bubbles appear rather irregular in their top views. Measuring 129 bubbles within 8 drops, we get an average area of 0.057 mm^2 with a standard deviation of 0.035 mm^2. The typical range of error in the bubble area measurements is ± 0.004 mm^2. Once the discrete large bubbles are formed, no appreciable changes in their size and shape were detected.

To achieve $R_m > R_o$, as shown in figure 3(*c*), we increase the Weber number from 25 to 106 as mentioned earlier. Then the spreading front becomes unstable because of the high Weber number (Kim, Feng & Chun 2000) and recedes upon reaching the maximum radius until it stops at the outer edge of the hydrophilic annulus (R_o). The entrainment of air takes place in a similar way to the process delineated above. Because this drop retains a higher kinetic energy than the previous one, its recoiling tends to be more vigorous, leaving the thin lens more vulnerable to disturbances that can lead to instability of the entire drop morphology. It is the trapped air bubbles that trigger the instability – a through-hole is nucleated by one of the bubbles as shown in 9.8 ms in figure 3(*c*), which then exposes the superhydrophobic area surrounded by the wettable annulus. The liquid that has covered the superhydrophobic area is completely disengaged from the surface (27.6 ms), leaving a water ring defined by the hydrophilic annulus.

The formation of a water ring followed by the ejection of liquid from a thin lens is the most peculiar aspect of the drop impact behaviour observed on a super-wettability-contrast annular pattern. Since liquid lenses containing air bubbles are commonly subjected to this instability, the lens shown in the last panel of figure 3(*b*) is also prone to bursting. In § 4, it will be explained under what conditions this bursting takes place.

4. Film rupture, liquid ejection, and water rings

On hydrophobic surfaces, thin water films easily dewet and break up into multiple sessile droplets when subjected to external disturbances. Any films with a thickness less than the critical value $h_c = 2l_c \sin(\theta_e/2)$, where the capillary length $l_c = \sqrt{\gamma/(\rho g)}$ and θ_e is the equilibrium contact angle, are unstable (de Gennes *et al.* 2004). For water-repellent surfaces, $h_c \approx 2l_c = 5.4$ mm, so the thin lenses obtained in this work, e.g. figure 3(*b*,*c*), with the maximum lens thickness of $\sim$80 μm can be destabilized easily. Furthermore, microbubbles trapped during the spreading phase aggravate the instabilities. For the drop of figure 3(*c*), a significant amount of kinetic energy remains even after initial spreading, which tends to perturb the drop leading to the immediate bursting of a hole. For water drops that do not burst upon spreading into a film, like the one in figure 3(*b*), we waited to see if any conformational change occurs while measuring the drop weight with a precision balance. The result was that every drop that formed a thin lens burst, so that the inner superhydrophobic area was exposed to air as shown in figure 6. The lens ruptures because the evaporating lens becomes unstable when its volume reaches a certain threshold value, which we estimate in the following.

We assume that the film instabilities manifest themselves when the free energy of a liquid lens penetrated by a hole, E_h, becomes lower than that of an undamaged lens, E_u, along the same lines as Sharma & Ruckenstein (1989). Figure 7 shows the

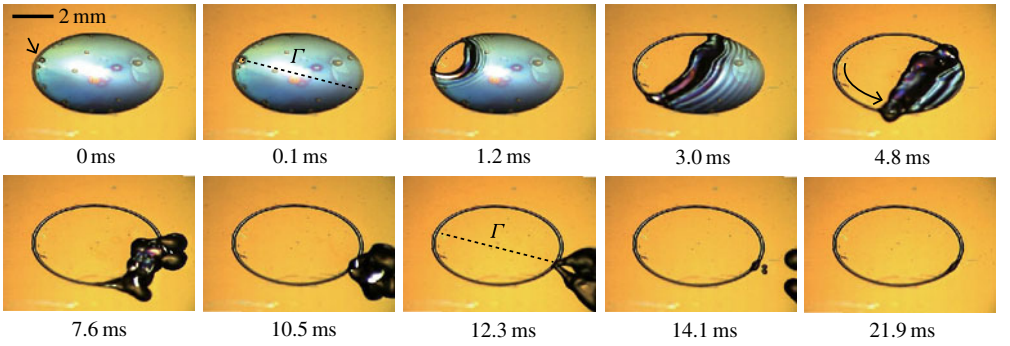

FIGURE 6. (Colour online) Bursting of a thin lens due to decrease of volume by evaporation, which eventually leads to the formation of a liquid ring. A bubble (indicated by an arrow) entrained in a liquid film at 0 ms generates a hole, which is detected by a high-speed camera in the next frame (0.1 ms).

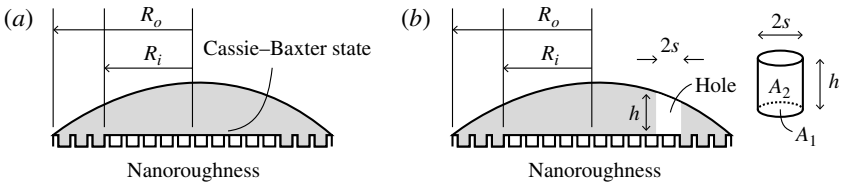

FIGURE 7. Schematic illustrations of liquid lenses on a super-wettability contrast surface with a wettable annular pattern. (*a*) Undamaged lens. (*b*) Lens penetrated by a hole of radius s located at the edge of the superhydrophobic circle.

schematics of liquid lenses sitting on surfaces with extreme wettability contrast. The radius of the liquid drop having the same volume as the bursting lens in this work ranges from 1.06 to 1.53 mm, and the maximum height of the lenses is less than 470 μm. Therefore, capillary forces dominate gravitational forces in determining the lens shape ($l_c = 2.7$ mm). This allows us to assume that the lenses are truncated spheres (de Gennes *et al.* 2004), consistent with our observation of their side views.

The undamaged lens, figure 7(*a*), is in contact with air at its top surface and touches the superhydrophilic annulus while supported by the tips of protrusions in the superhydrophobic area, locally achieving the Cassie–Baxter state. For the damaged lens, figure 7(*b*), we assume that a cylindrical hole with bottom area A_1 and side area A_2 emerges near the edge of the inner superhydrophobic area, based on our experimental observation that relatively large air bubbles are trapped at the wettability boundary. Neglecting the change of the overall lens shape with a hole, whose volume is very small compared to that of the lens, we write

$$\Delta E = E_h - E_u = \gamma\,[A_2 - A_1(1 - \cos\theta_C)]\,. \tag{4.1}$$

Here we used the Cassie–Baxter equation, which gives the apparent contact angle of the Cassie–Baxter state, θ_C, as $\gamma\cos\theta_C = \phi(\gamma_{SG} - \gamma_{SL}) - (1-\phi)\gamma$, where ϕ is the wetted fraction of the solid area, and γ_{SL} and γ_{SG} are the solid–liquid and solid–gas interfacial energy per unit area, respectively. Above we ignored gravitational potential energies in view of the small thickness of the drop compared to the capillary length.

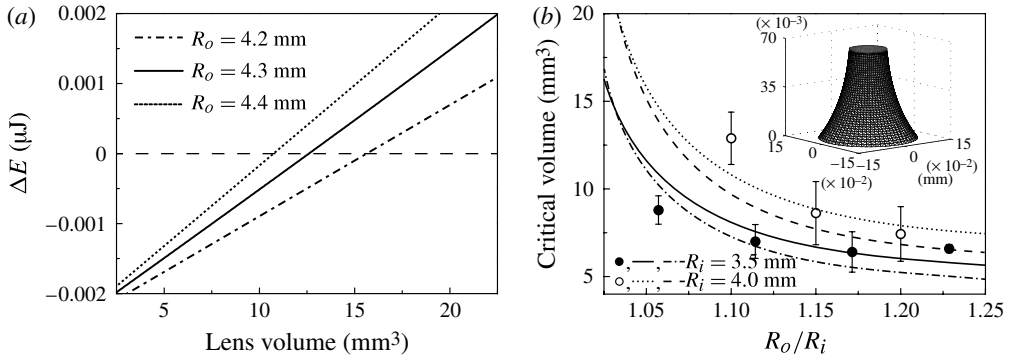

FIGURE 8. (*a*) ΔE versus the lens volume for $[R_i, s] = [4, 0.075]$ mm. (*b*) Critical volumes at which a hole bursts. The solid and dotted lines are the theoretical predictions using the cylindrical hole assumption. The dashed and dot-dashed lines are the theoretical predictions for the holes satisfying the Young–Laplace equation. The circles are the measurement results. The inset is the hole shape satisfying the Young–Laplace equation for a lens on the annulus pattern with $[R_i, R_o] = [3.5, 4.1]$ mm.

Also, the hole was assumed to be a circular cylinder to facilitate the evaluation of A_2. For a cylindrical hole with a radius s, $A_1 = \pi s^2$ and $A_2 = 2\pi sh$. Here h is taken to be a representative height of the cylindrical hole, as shown in figure 7(*b*):

$$h = \sqrt{R_c^2 - (R_i - s)^2} - R_c + H, \tag{4.2}$$

where R_c and H are the radius of curvature and the maximum height of the drop at its critical volume for hole nucleation, respectively.

Plotting ΔE versus the lens volume V in figure 8(*a*), we find that ΔE becomes negative as V decreases, indicating that a small lens with a hole becomes energetically more favourable than undamaged ones. We compare the experimentally measured critical volumes that initiate the hole burst with the theoretical predictions (solid and dotted lines) in figure 8(*b*), which shows reasonable agreement between experiment and theory with a fitting parameter $s = 75$ μm, which is slightly smaller than the radius of a hole (∼90 μm) first detected by the high-speed camera (0.1 ms in figure 6). We also included the theoretical results with the hole shape obtained by solving the Young–Laplace equation (dashed and dot-dashed lines) in figure 8(*b*). In the calculation, the bottom of the hole was assumed to retain the contact angle of 160°, the interfacial energies of the lenses with and without the hole were set to be identical, and the average hole radius was taken to be 75 μm. A hole satisfying the Young–Laplace equation for a lens on the annulus pattern with $[R_i, R_o] = [3.5, 4.1]$ mm is shown in the inset of figure 8(*b*). The modelling results using a cylindrical hole and a hole satisfying the Young–Laplace equation are shown to differ at most 14 % for the same annulus dimensions. At fixed R_i, the critical volume decreases as R_o increases; thus a lens formed on a wider annulus (large R_o/R_i) can get thinner before bursting than one formed on a narrower annulus (small R_o/R_i).

Once a hole emerges, it expands along the inner edge of the hydrophilic annulus as it cannot interrupt the intimate contact between the liquid and the hydrophilic solid. The distance that the hole sweeps along the inner edge, as indicated by an arrow in the fifth panel of figure 6, turns out to increase linearly with time, giving a constant hole expansion speed, U_h, for each experimental condition. U_h ranges

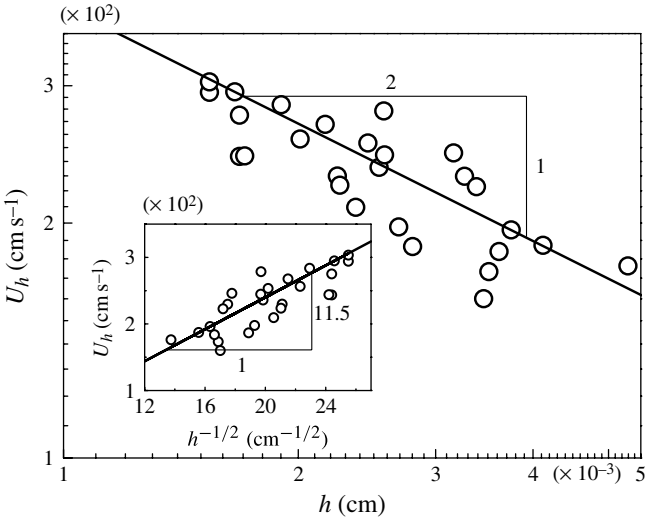

FIGURE 9. Speed of hole expansion U_h versus h for various values of initial drop volume, R_i and R_o. The inset plots U_h versus $h^{-1/2}$ to find the proportionality constant to be 11.5.

from 1.5 to 3 m s^{-1} in this work. The corresponding Reynolds number $Re_h = \rho U_h h/\mu$ ranges from 41 to 96. The hole opening is driven by the capillarity but resisted by inertia. If a hole is nucleated at the centre of a liquid disk, the capillary force driving the hole expansion is given by $F_d = 2\pi r_h \gamma(1 - \cos\theta_C)$, where r_h is the hole radius. Balancing F_d with the resisting force due to inertia, $F_r = 2\pi\rho r_h \tilde{h} U_h^2$, gives the hole opening speed $U_h = [\gamma(1 - \cos\theta_C)/(\rho\tilde{h})]^{1/2}$, where $\tilde{h}$ is the nominal film thickness. For a film floating in the air ($\theta_C = 180°$), we get the Taylor–Culick formula, $U_h = [2\gamma/(\rho\tilde{h})]^{1/2}$ (Taylor 1959; Culick 1960; de Gennes *et al.* 2004). For the present superhydrophobic surface with $\theta_C = 160°$, the numerical prefactor changes but slightly, giving $U_h \approx 12\tilde{h}^{-1/2}$, with U_h and $\tilde{h}$ having the units of cm s^{-1} and cm, respectively. Although the hole in this work is nucleated near the edge of the lens rather than the centre, our experimental measurements of U_h do indeed reveal that U_h is scaled as $h^{-1/2}$, as shown in figure 9. Here we have taken $\tilde{h} = h$. The inset of the figure finds the proportionality constant to be 11.5 via the least-squares method, a value surprisingly close to the one derived for a hole opening from the centre.

Because the film gets thicker towards the centre, corresponding to lower U_h, the hole opens along the edge first. This causes the central droplet to be completely separated from the surrounding rim adhering to the hydrophilic annulus. As the central part of the lens transforms into a sphere due to surface tension effect, its excess energy, i.e. the difference of the potential energies of the lens and the sphere, is partly converted to the translational kinetic energy. This allows the droplet to disengage from the water-repellent surface, or jump.

We note that the path of the liberated droplet projected onto the solid surface exactly overlaps with a line Γ that connects the hole nucleation site and the centre of the annulus, as illustrated in figure 6 (0.1 and 12.3 ms). It is because the hole expansion and resulting film lift is symmetric about the line Γ before it loses contact with the intersection of the line Γ and the annulus. The take-off angle β is closely associated

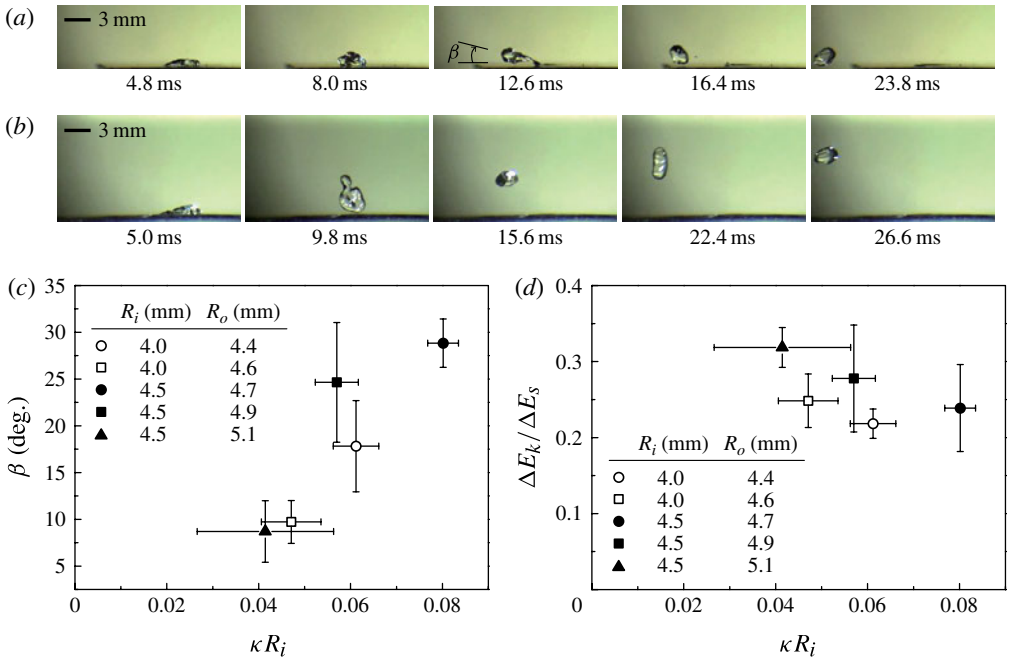

FIGURE 10. (Colour online) (*a*) Ejection of a droplet from a relatively flat liquid lens. $[R_i, R_o] = [4.0, 4.6]$ mm. (*b*) Ejection of a droplet from a relatively curved liquid lens. $[R_i, R_o] = [4.5, 4.7]$ mm. (*c*) The take-off angle (β) versus the lens slope (κR_i). (*d*) The kinetic to surface energy ratio versus the lens slope.

with the relative speed of hole opening to film flotation. As shown in figure 10(*a*), when the lens is relatively flat for its large area of inner circle (large R_i) or wide annulus (large R_o/R_i), the hole opening along the edge and the retraction of the film occur almost at the same rate because of the relatively uniform thickness throughout the lens. Thus, the droplet is ejected almost parallel to the solid surface, yielding a very low β, 7°. On the other hand, for a highly curved lens with a small area of inner circle (small R_i) or narrow annulus (small R_o/R_i) (figure 10*b*), the hole opening is much faster than the film retraction toward the centre. The difference in the speeds of hole opening and film retraction is caused by a relatively large difference of the film thicknesses near the wettability boundary and at the centre. Thus, the central film is quickly separated from the rim before being lifted in the air. Then the isolated liquid mass jumps off the surface forming a spherical droplet with a high β, 31°. We plot the experimentally measured values of β versus the characteristic slope, κR_i, of the lenses assumed to be a truncated sphere in figure 10(*c*), to find that β is strongly correlated with κR_i. Here κ is the curvature of the bursting lens.

By comparing the surface energy change of a liquid mass associated with separation from the rim and its kinetic energy at take-off, it is possible to evaluate how much energy is dissipated during the droplet ejection process. The reduction of the surface energy as liquid transforms from a sessile film to a floating sphere corresponds to $\Delta E_s = \pi R_i^2 \gamma (1 - \cos\theta_C) - 4\pi r_d^2 \gamma$, where r_d is the radius of the spherical droplet ejected from the lens. Here, the surface area of the spherical lens exposed to air, $A_u = \pi R_i^2 [1 + (H - h)^2 / R_i^2]$, is simply approximated to be $A_u \approx \pi R_i^2$

because $(H-h)^2/R_i^2$ is of the order of 10^{-2}. With the take-off speed of the droplet v_d, the kinetic energy is written as $\Delta E_k = (2\pi/3)\rho r_d^3 v_d^2$. In our experiments, r_d varies from 0.80 to 1.24 mm and v_d from 0.68 to 1.45 m s^{-1}. Figure 10(*d*) plots the energy conversion ratio, $\Delta E_k/\Delta E_s$, versus the characteristic slope κR_i. Unlike the take-off angle, the energy conversion ratio tends to decrease with κR_i. It is attributed to the shape of ejected droplets that depends on the take-off angle or κR_i. The droplet shape is highly irregular upon take-off for high κR_i, e.g. the one in 9.8 ms in figure 10(*b*), while it is close to spherical for low κR_i, e.g. the one in 16.4 ms in figure 10(*a*). Therefore, the surface energy of droplets ejected from highly curved lenses is converted into vibrational and viscous energy in addition to translational kinetic energy (Biance *et al.* 2006), lowering the ratio $\Delta E_k/\Delta E_s$, from approximately 0.3 to 0.2.

The jumping of drops on superhydrophobic surfaces has been reported in several other situations as well. Drops impacting on a uniformly superhydrophobic surface rebound vertically (Richard & Quéré 2000), whereas those colliding with non-uniform wettability would rebound obliquely because of the difference in dewetting speeds around the rim of squeezed drops. Reyssat, Pardo & Quéré (2009) observed the oblique rebound of water drops hitting micropillar arrays with gradients of pillar density, where the take-off angle could be varied from 90° to approximately 60°. In addition, tiny droplets undergoing coalescence (Boreyko & Chen 2009) and melting (Habenicht *et al.* 2005) can jump off water-repellent surfaces. The high-speed imaging of Boreyko & Chen revealed that condensate water drops with a diameter of the order of 10^2 μm merge and almost vertically jump off a superhydrophobic surface with a velocity of the order of 0.1 m s^{-1}. Comparing with those previous investigations of droplet jumps off the surface, we find that the current work achieves the lowest take-off angle, which may be useful where violent droplet behaviour needs to be avoided, e.g. within a small lab-on-a-chip system.

Finally we consider the volume and stability of the ring that remains after film burst. We assume that the cross-section of the ring is a truncated circle because the Bond number $Bo = \rho g b^2/\gamma \sim 10^{-5}$, where b is the maximum thickness within the ring. Then the volume of the ring, V_r, is related to the apparent contact angle of the ring, θ_0, as

$$V_r = \frac{\pi}{2}(R_i + R_o)\left(\frac{R_o - R_i}{2\sin\theta_0}\right)^2 (2\theta_0 - \sin 2\theta_0). \tag{4.3}$$

Our experiments reveal that θ_0 ranges between 2° and 28°. We found qualitatively that V_r and θ_0 tend to increase as κR_i decreases (or as β decreases). This tendency is because a stretched liquid bridge trailing the ejected droplet, as shown at 12.6 ms in figure 10(*a*), partly recoils back to the ring at low β. Such recoiling of the bridge increases the volume of remaining ring. When the liquid ring is bound by the pre-defined hydrophilic annulus, the contact line is pinned, and thus the ring is stable, i.e. no beading occurs, for $\theta_0 < \pi/2$ (Davis 1980; Schiaffino & Sonin 1997), which is consistent with our observations. For $\theta_0 > \pi/2$, the liquid thread is known to be subjected to capillary instability. Because of the low contact angle of the rings produced in this work, the rings remain stable until they are dried off and dry spots appear.

5. A practical implication

The wettability contrast can be explored to generate liquid patterns on solid surfaces for rapid printing of electronic circuits (Russo *et al.* 2011) and biological fluids

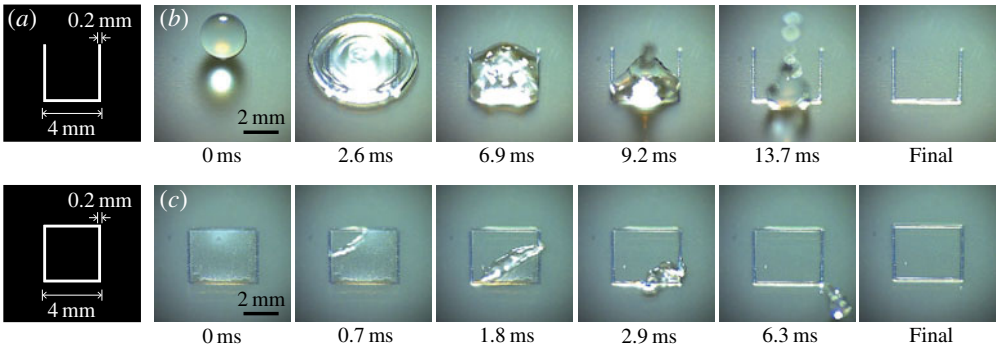

FIGURE 11. (Colour online) Rapid printing of a liquid deposit using wettability-contrast patterns. (*a*) Photomask pattern used to print liquid on solids. (*b*) Printing of water on the wettability-patterned surface that is tilted 16° from the horizontal. The drop is easily removed from the hydrophobic region when the hydrophilic curve is open. (*c*) Printing of closed curves using spontaneous film rupture.

(Roth *et al.* 2004). As shown in figure 11, liquid lines and curves can be easily drawn by impacting a liquid drop on a tilted substrate. Starting from a photomask with a desired pattern (figure 11*a*), we perform photolithography on a uniformly superhydrophobic surface in the same manner as figure 1. Then the hydrophobic substrate is selectively treated to turn hydrophilic in desired areas. Upon drop impact, while the liquid is rapidly drained down the substrate, the contact lines are arrested on hydrophilic patterns thereby allowing the liquid to be patterned along the pre-defined hydrophilic areas as shown in figure 11(*b*). Despite being a promising method to print functional liquids on solids, this method may cause a serious problem in drawing closed curves if the liquid covering the inner region fails to be drained. The behaviour of a liquid film investigated in this work provides a viable solution to this problem – thin films arrested by hydrophilically treated closed curves are unstable, and thus spontaneously rupture to expose the hydrophobic inner regions, as shown in figure 11(*c*). The liquid ejection behaviour from the rectangular wettable loop is similar to what is observed for the circular loops.

It is noted that most functional liquids, including conducting liquids and biological fluids, may have higher viscosity and lower surface tension than pure water, providing more resistance and lower driving forces to the film rupture. By testing the bursting behaviour of water–glycerine mixtures (36 wt% glycerine, $\mu = 3.1$ mPa s, $\gamma = 68.2$ N m^{-1}) on an annulus pattern with $R_i = 4.0$ and $R_o = 4.4$ mm, the liquid film is found to still burst when its volume is decreased by evaporation just as a pure water deposit does. However, the threshold volume for the burst is measured to be 71 % that of water, implying that water–glycerine films burst at a smaller thickness than water films. Also, the film rupture speed is found to be only 16 % that of water, hinting at a retardation effect of increased μ and decreased γ on bursting.

6. Conclusions

We have shown that drops impacting on super-wettability-contrast annular patterns exhibit novel dynamic behaviours that are distinguished from ones on surfaces with uniform wettability. The liquid film covering the superhydrophobic region as arrested by the hydrophilic annulus is spontaneously ruptured to completely disengage from

the surface leading to the formation of a water ring. The critical volume of the film for hole formation and the take-off angle and energy conversion ratio of the ejected droplet have been quantified. The practical implication that this phenomenon has in association with the printing of functional liquids has been demonstrated.

The jumping of drops on superhydrophobic surfaces, reported here and in several other situations (Richard & Quéré 2000; Boreyko & Chen 2009; Habenicht *et al.* 2005), are commonly due to a severe difference between the surface energy of a deposit on a solid surface and that of a floating drop of identical mass. The surface energy difference is released in the form of translational and vibrational kinetic energy. The ejection of part of a liquid lens, as observed in this work, serves as another novel example of strong water repulsion dynamics. Also, the ejection of water controlled by the liquid film mass (varied via evaporation in this work) provides a novel pathway to achieving jetting of liquids resting on solids, which has so far mainly been explored using electrohydrodynamic effects (Collins *et al.* 2008; Kim *et al.* 2011*c*).

Acknowledgement

This work was supported by the National Research Foundation of Korea (grants 2011-0030744 and 2012-008023) via SNU-IAMD.

REFERENCES

Biance, A.-L., Chevy, F., Clanet, C., Lagubeau, G. & Quéré, D. 2006 On the elasticity of an inertial liquid shock. *J. Fluid Mech.* **554**, 47–66.

Bico, J., Tordeux, C. & Quéré, D. 2001 Rough wetting. *Europhys. Lett.* **55**, 214–220.

Blake, T. D. & Ruschak, K. J. 1979 A maximum speed of wetting. *Nature* **282**, 489–491.

Boreyko, J. B. & Chen, C.-H. 2009 Self-propelled dropwise condensate on superhydrophobic surfaces. *Phys. Rev. Lett.* **103**, 184501.

Cassie, A. B. D. & Baxter, S. 1944 Wettability of porous surfaces. *Trans. Faraday Soc.* **40**, 546–551.

Clanet, C., Béguin, C., Richard, D. & Quéré, D. 2004 Maximal deformation of an impacting drop. *J. Fluid Mech.* **517**, 199–208.

Collins, R. T., Jones, J. J., Harris, M. T. & Basaran, O. A. 2008 Electrohydrodynamic tip streaming and emission of charged drops from liquid cones. *Nat. Phys.* **4**, 149–154.

Courbin, L., Denieul, E., Dressaire, E., Roper, M., Ajdari, A. & Stone, H. A. 2007 Imbibition by polygonal spreading on microdecorated surfaces. *Nat. Mater.* **6**, 661–664.

Cubaud, T. & Fermigier, M. 2001 Faceted drops on heterogeneous surfaces. *Europhys. Lett.* **55**, 239–245.

Culick, F. E. C. 1960 Comments on a ruptured soap film. *J. Appl. Phys.* **31**, 1128–1129.

Davis, S. H. 1980 Moving contact lines and rivulet instabilities. Part 1. The static rivulet. *J. Fluid Mech.* **98**, 225–242.

Duez, C., Ybert, C., Clanet, C. & Bocquet, L. 2007 Making a splash with water repellency. *Nat. Phys.* **3**, 180–183.

Eggers, J. 2004 Hydrodynamic theory of forced dewetting. *Phys. Rev. Lett.* **93**, 094502.

de Gennes, P.-G., Brochard-Wyart, F. & Quéré, D. 2004 *Capillarity and Wetting Phenomena: Drops, Bubbles, Pearls, Waves*. Springer.

Habenicht, A., Olapinski, M., Burmeister, F., Leiderer, P. & Boneberg, J. 2005 Jumping nanodroplets. *Science* **309**, 2043–2045.

Ishino, C., Reyssat, M., Reyssat, E., Okumura, K. & Quéré, D. 2007 Wicking within forests of micropillars. *Europhys. Lett.* **79**, 56005.

Jokinen, V., Sainiemi, L. & Franssila, S. 2008 Complex droplets on chemically modified silicon nanograss. *Adv. Mater.* **20**, 3453–3456.

KATAOKA, D. E. & TROIAN, S. M. 1999 Patterning liquid flow on the microscopic scale. *Nature* **402**, 794–797.

KIM, P., DUPRAT, C., TSAI, S. S. H. & STONE, H. A. 2011*c* Spreading and jetting of electrically driven dielectric films. *Phys. Rev. Lett.* **107**, 034502.

KIM, H.-Y., FENG, Z. C. & CHUN, J.-H. 2000 Instability of a liquid jet emerging from a droplet upon collision with a solid surface. *Phys. Fluids* **12**, 531–541.

KIM, S. J., MOON, M.-W., LEE, K.-R., LEE, D.-Y., CHANG, Y. S. & KIM, H.-Y. 2011*a* Liquid spreading on superhydrophilic micropillar arrays. *J. Fluid Mech.* **680**, 477–487.

KIM, J., MOON, M.-W., LEE, K.-R., MAHADEVAN, L. & KIM, H.-Y. 2011*b* Hydrodynamics of writing with ink. *Phys. Rev. Lett.* **107**, 264501.

LEE, M., CHANG, Y. S. & KIM, H.-Y. 2010 Drop impact on microwetting patterned surfaces. *Phys. Fluids* **22**, 072101.

MAO, T., KUHN, D. C. S. & TRAN, H. 1997 Spread and rebound of liquid droplets upon impact on flat surfaces. *AIChE J.* **43**, 2169–2179.

ONDA, T., SHIBUICHI, S., SATOH, N. & TSUJII, K. 1996 Super-water-repellent fractal surfaces. *Langmuir* **12**, 2125–2127.

QUÉRÉ, D. 2008 Wetting and roughness. *Annu. Rev. Mater. Res.* **38**, 71–99.

REIN, M. 1993 Phenomena of liquid drop impact on solid and liquid surfaces. *Fluid Dyn. Res.* **12**, 61–93.

REYSSAT, M., PARDO, F. & QUÉRÉ, D. 2009 Drops onto gradients of texture. *Europhys. Lett.* **87**, 36003.

RICHARD, D. & QUÉRÉ, D. 2000 Bouncing water drops. *Europhys. Lett.* **50**, 769–775.

RIOBOO, R., VOUÉ, M., VAILLANT, A. & DE CONINCK, J. 2008 Drop impact on porous superhydrophobic polymer surfaces. *Langmuir* **24**, 14074–14077.

ROTH, E. A., XU, T., DAS, M., GREGORY, C., HICKMAN, J. J. & BOLAND, T. 2004 Inkjet printing for high throughput cell patterning. *Biomaterials* **25**, 3707–3715.

RUSSO, A., AHN, B. Y., ADAMS, J. J., DUOSS, E. B., BERNHARD, J. T. & LEWIS, J. A. 2011 Pen-on-paper flexible electronics. *Adv. Mater.* **23**, 3426–3430.

SBRAGAGLIA, M., PETERS, A. M., PIRAT, C., BORKENT, B. M., LAMMERTINK, R. G. H., WESSLING, M. & LOHSE, D. 2007 Spontaneous breakdown of superhydrophobicity. *Phys. Rev. Lett.* **99**, 156001.

SCHIAFFINO, S. & SONIN, A. A. 1997 Formation and stability of liquid and molten beads on a solid surface. *J. Fluid Mech.* **343**, 95–110.

SHARMA, A. & RUCKENSTEIN, E. 1989 Dewetting of solids by the formation of holes in macroscopic liquid films. *J. Colloid Interface Sci.* **133**, 358–368.

SHIN, B., LEE, K.-R., MOON, M.-W. & KIM, H.-Y. 2012 Extreme water repellency of nanostructured low-surface-energy non-woven fabrics. *Soft Matt.* **8**, 1817–1823.

TAYLOR, G. I. 1959 The dynamics of thin sheets of fluid. Part 3. Disintegration of fluid sheets. *Proc. R. Soc. London. Ser.* A **253**, 313–321.

TSAI, P., PACHECO, S., PIRAT, C., LEFFERTS, L. & LOHSE, D. 2009 Drop impact upon micro- and nanostructured superhydrophobic surfaces. *Langmuir* **25**, 12293–12298.

WENZEL, R. N. 1936 Resistance of solid surfaces to wetting by water. *Ind. Engng Chem.* **28**, 988–994.

WORTHINGTON, A. M. 1877 On the forms assumed by drops of liquid falling on a horizontal plate. *Proc. R. Soc. London* **25**, 261–272.

YARIN, A. L. 2006 Drop impact dynamics: splashing, spreading, receding, bouncing. *Annu. Rev. Fluid Mech.* **38**, 159–192.

ZHANG, Y., ZHU, Y., YAO, B. & FANG, Q. 2011 Nanolitre droplet array for real time reverse transcription polymerase chain reaction. *Lab on a Chip* **11**, 1545–1549.

ZHAO, B., MOORE, J. S. & BEEBE, D. J. 2001 Surface-directed liquid flow inside microchannels. *Science* **291**, 1023–1026.